

Creation and diagnosis of a solid-density plasma with an X-ray free-electron laser

S. M. Vinko¹, O. Ciricosta¹, B. I. Cho², K. Engelhorn², H.-K. Chung³, C. R. D. Brown⁴, T. Burian⁵, J. Chalupský⁵, R. W. Falcone^{2,6}, C. Graves⁷, V. Hájková⁵, A. Higginbotham¹, L. Juha⁵, J. Krzywinski⁷, H. J. Lee⁷, M. Messerschmidt⁷, C. D. Murphy¹, Y. Ping⁸, A. Scherz⁷, W. Schlotter⁷, S. Toleikis⁹, J. J. Turner⁷, L. Vysin⁵, T. Wang⁷, B. Wu⁷, U. Zastrau¹⁰, D. Zhu⁷, R. W. Lee⁷, P. A. Heimann², B. Nagler⁷ & J. S. Wark¹

Matter with a high energy density ($>10^5$ joules per cm^3) is prevalent throughout the Universe, being present in all types of stars¹ and towards the centre of the giant planets^{2,3}; it is also relevant for inertial confinement fusion⁴. Its thermodynamic and transport properties are challenging to measure, requiring the creation of sufficiently long-lived samples at homogeneous temperatures and densities^{5,6}. With the advent of the Linac Coherent Light Source (LCLS) X-ray laser⁷, high-intensity radiation ($>10^{17}$ watts per cm^2 , previously the domain of optical lasers) can be produced at X-ray wavelengths. The interaction of single atoms with such intense X-rays has recently been investigated⁸. An understanding of the contrasting case of intense X-ray interaction with dense systems is important from a fundamental viewpoint and for applications. Here we report the experimental creation of a solid-density plasma at temperatures in excess of 10^6 kelvin on inertial-confinement time-scales using an X-ray free-electron laser. We discuss the pertinent physics of the intense X-ray-matter interactions, and illustrate the importance of electron-ion collisions. Detailed simulations of the interaction process conducted with a radiative-collisional code show good qualitative agreement with the experimental results. We obtain insights into the evolution of the charge state distribution of the system, the electron density and temperature, and the time-scales of collisional processes. Our results should inform future high-intensity X-ray experiments involving dense samples, such as X-ray diffractive imaging of biological systems, material science investigations, and the study of matter in extreme conditions.

The experiment was performed at the LCLS soft X-ray materials science instrument (SXR), where a 1.0- μm -thick aluminium (Al) foil was irradiated with 80-fs X-ray pulses at photon energies in the range 1,560–1,830 eV (at and above the Al K edge). The LCLS pulse contained $\sim 10^{12}$ photons with an energy bandwidth of $\sim 0.4\%$. The X-ray pulse was focused by means of bendable Kirkpatrick-Baez mirrors, and the focal spot was characterized *ex situ* by analysing imprints in lead tungstate (ref. 9), indicating a spot size of $9.1 \pm 0.8 \mu\text{m}^2$, that is, a peak intensity of $1.1 \times 10^{17} \text{ W cm}^{-2}$. Aluminium was studied because it is a prototypical free-electron metal, presenting all the intricacies of a high-electron-density system, yet possessing a relatively simple atomic structure. Our main target diagnostic is X-ray emission spectroscopy, sensitive to recombination from the L to the K shell, that is, to Al K α emission, in the spectral range 1,460–1,680 eV.

The absorption process in the Al foil is dominated by K-shell photoabsorption, ejecting a core electron into the continuum, because the cross-section for L-shell and valence-band photoionization is over a factor 10 smaller. After photoionization, the filling of the K-shell hole proceeds mainly by KLL Auger decay, producing an ion with two holes in the L shell. Radiative emission accounts for the remaining 3.8% of

the total recombination from the L shell¹⁰. In Fig. 1 we plot the spectrally resolved X-ray emission over a range of excitation photon energies between 1,560 and 1,830 eV. The spectra show the main K α peak around 1,487 eV, followed by a series of peaks corresponding to emission from higher charge states due to a growing number of L-shell holes.

The observation of K α emission from highly charged ions in a dense system is not of itself novel, being routinely observed when charged-particle beams (such as ions or optical-laser-generated energetic electrons) interact with solid targets^{11–17}. However, our results differ from these experiments in two important ways. First, in our experiment the K-shell holes are created exclusively by intense, quasi-monochromatic X-ray photons rather than by collisions with broadband energetic particles. The main absorption process (creating K-shell holes) will therefore only take place in a particular ion if the photon energy lies above that ion's K edge, or, given that the X-rays are so intense, if a K electron is resonantly pumped to a vacant L-shell state. It follows that the X-ray free-electron laser (FEL) acts not only as a pump—exciting electrons and heating the system—but also as a selective probe, in that

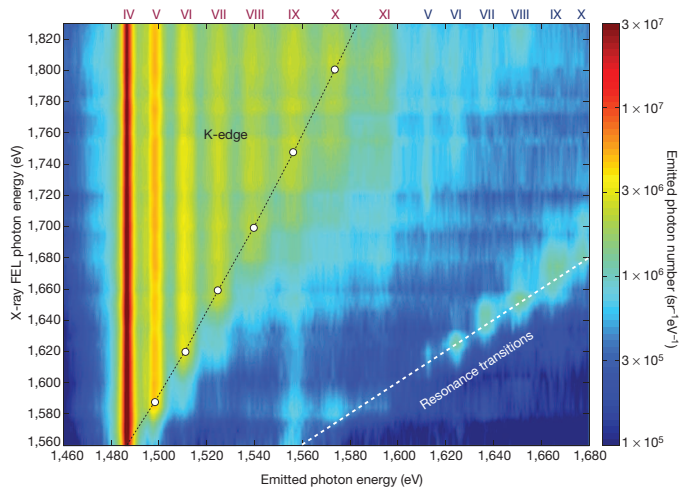


Figure 1 | Spectrally resolved K α emission as a function of the X-ray FEL excitation photon energy. The colour coding (bar on right) refers to the emission intensity on a logarithmic scale. Roman numerals (top) indicate the charge state of the emission peak: red, for states with a single K-shell hole; blue, for states with a double K-shell hole. Peaks around the resonance line (dashed white line, indicating where the FEL photon energy equals the emitted photon energy) correspond to emission from resonantly-pumped K–L transitions. Open circles, K edges for the various charge states calculated in the SCFLY code, which includes the ionization potential depression in the dense plasma according to a modified version of the Stewart-Pyatt model^{21,22}.

¹Department of Physics, Clarendon Laboratory, University of Oxford, Parks Road, Oxford OX1 3PU, UK. ²Lawrence Berkeley National Laboratory, 1 Cyclotron Road, California 94720, USA. ³Atomic and Molecular Data Unit, Nuclear Data Section, IAEA, PO Box 100, A-1400, Vienna, Austria. ⁴Plasma Physics Department, AWE Aldermaston, Reading RG7 4PR, UK. ⁵Institute of Physics ASCR, Na Slovance 2, 18221 Prague 8, Czech Republic. ⁶Department of Physics, University of California, Berkeley, California 94720, USA. ⁷SLAC National Accelerator Laboratory, 2575 Sand Hill Road, Menlo Park, California 94025, USA. ⁸Lawrence Livermore National Laboratory, 7000 East Avenue, Livermore, California 94550, USA. ⁹Deutsches-Elektronensynchrotron DESY, Notkestrasse 85, 22603 Hamburg, Germany. ¹⁰IQO, Friedrich-Schiller-Universität Jena, Max-Wien-Platz 1, 07743 Jena, Germany.

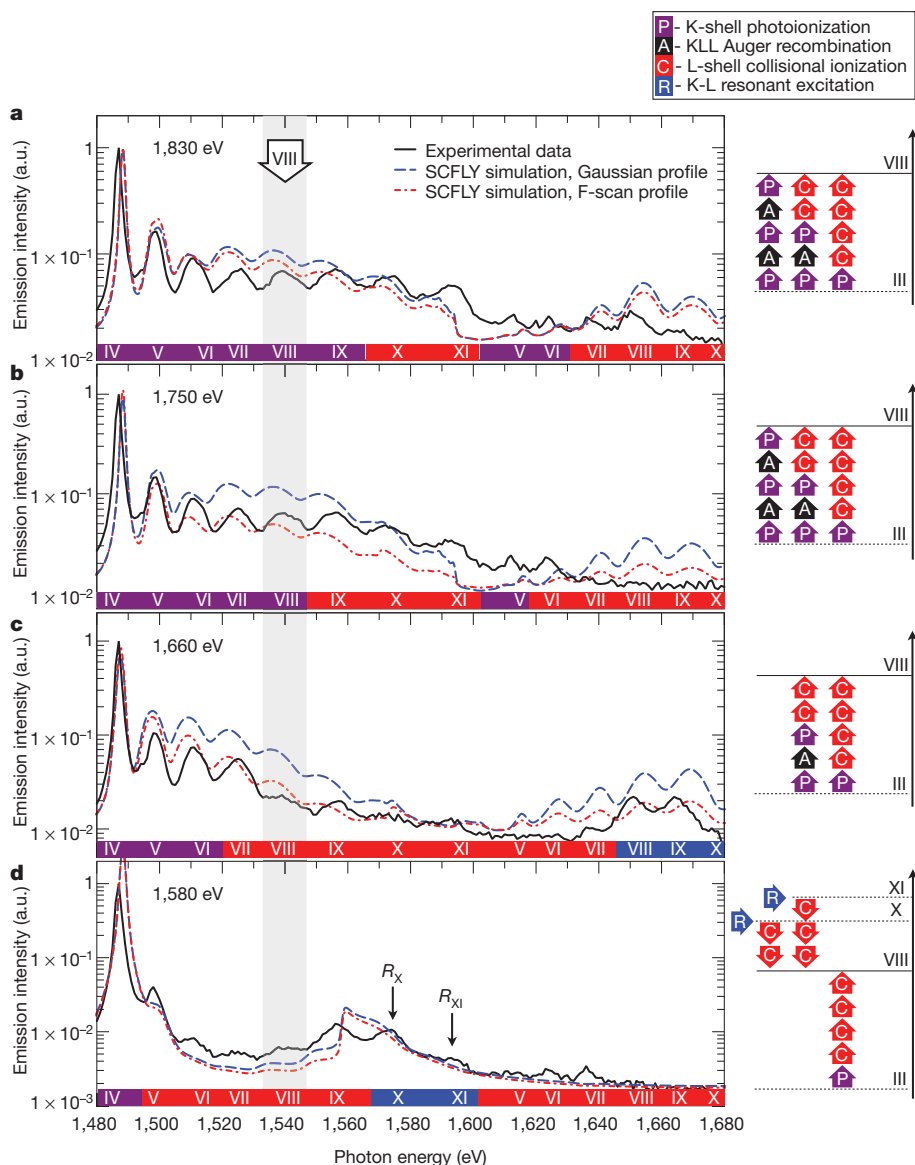


Figure 2 | Experimental and theoretical spectra, and charge-state emission pathways. Left, calculated emission spectra (dashed lines) according to the SCFLY code for four X-ray energies (a, 1,830 eV; b, 1,750 eV; c, 1,660 eV; d, 1,580 eV), compared with the experimental results presented in Fig. 1 (solid lines). The two simulation curves correspond to different X-ray intensity distributions on target: a Gaussian profile and the measured F-scan profile. Also shown (right) are the various pathways leading to emission from an ion with five L-shell holes in the final state (VIII), observed as the fifth emission peak: these pathways depend strongly on the wavelength of the X-ray excitation. R_X and R_{XI} correspond to emission from resonant transitions between K- and L-shell states in an ion containing seven or eight L-shell holes, respectively (states X and XI). Colour bars below each plot on left indicate the dominant mechanism contributing to the emission intensity for the various charge states (Roman numerals). a.u., arbitrary units.

the K-shell holes and subsequent $K\alpha$ emission only occur from a select range of ion charge states, depending on the FEL photon energy. As shown in Fig. 1, the range of ions from which we see K-shell emission is indeed strongly dependent on the energy of the incident photon: at photon energies just above the neutral K edge only a limited number of ionization stages is observed, whereas at the highest photon energy of 1,830 eV we observe all possible ionization stages corresponding to the filling of a single K-shell hole. In addition, at specific photon pump energies, we observe emission from resonantly pumped single- and double-hole K-shell states, marked as resonance transitions in Fig. 1. We label all emission peaks according to their K- and L-shell charge state (the three M-shell electrons are free-electron-like in ground-state Al): that is, the main $K\alpha$ peak corresponds to charge state IV and the higher energy peaks correspond to states in the range V–XI. The second important difference to note is that in our experiment the population of L-shell states, and the charge state distribution (CSD), is seen to be determined predominantly by electron–ion collisional processes within the heated dense system, rather than directly by the X-ray pulse. Therefore, provided the photon energy is sufficiently high to satisfy the probe condition described above for all charge states, the $K\alpha$ emission spectrum contains information on the CSD of the hot system, on the electron temperature and on electron–ion collision rates (best observed in the case of resonances where not one but several emission peaks are observed at a single pump energy).

This pivotal role of collisions in determining the observed spectra and the CSD is evinced by two main features in the data. The first is the relatively uniform intensity of the $K\alpha$ emission as a function of charge state. For isolated atoms, successive sequential photoionization of the K-shell occurs, with the dominant ionization pathway being a P-A-P-A... process (where P indicates photoionization, and A Auger decay)⁸. As each P-A sequence results in two electrons being ejected from the L shell, the populations of ions with an even number of ejected electrons dominate over those with an odd number ejected. In contrast, for the solid-density system, the dynamics are distinctly different, and we observe no odd–even asymmetry in the $K\alpha$ emission. This is due to the high electron–ion collision rates, which compete with both the P and A processes. Our simulations (below) show that the collisional and Auger rates are comparable at the peak of the pulse at the highest intensities. The second piece of evidence for the important role of collisions is the observation of emission corresponding to resonantly pumped single and double-core-hole states in ion stages for which direct photo-ionization of a K-shell electron is energetically forbidden. As the number of electrons in the L shell decreases, the reduced screening results in tighter binding of the K electrons, increasing the K-edge energy as a function of ion stage (see Fig. 1). Thus, for a particular photon energy, the ejection of a K electron is only possible up to a certain ion stage, explaining the observed fundamental trend where $K\alpha$ emission is seen from higher charge states as the photon energy is

increased. Nevertheless, this principle can be violated, as the density is so high that additional collisional ionization occurs, promoting further L electrons to the continuum (in addition to those ionized by Auger recombination). Such collisional ionization takes place for ions with two K electrons present and, importantly, is also sufficiently rapid that it can produce further L-shell vacancies in ions already containing a K-shell hole (that is, after photoabsorption, yet before Auger or radiative decay). In the former case, ions with K-edge energies higher than the incident photon energy can be created, but further photo-excitation of K-shell electrons to the continuum for these ions is no longer possible, as the K edge exceeds the photon energy. In the latter case, two interesting effects arise.

First, some $K\alpha$ emission is still seen from ion stages which have K-edge energies higher than the photon energy, via a process whereby photo-excitation of the K shell occurs at a lower ion stage, collisions ionize further L-shell electrons in the presence of the K-shell hole, then radiative decay occurs producing $K\alpha$ emission. This effect can be seen in Fig. 1 by comparing the spectrum for a given LCLS photon energy with the calculated energy of the K edge for a particular ion stage. Although accurate independent measurements of the K-edge positions in these hot-dense conditions are not available (we note that our results provide some information in this regard, albeit blurred by strong collisional effects), forcing us to rely on computational modelling, we note that in order to explain the spectra in terms of a K-edge shift alone in the absence of collisional ionization, the calculated shifts would need to be incorrect by several hundred electron volts for the highest charge states. Such a large discrepancy is implausible, but more importantly, would also lead to severely inconsistent simulation results for the emission spectrum. We further note that this observation also cannot be explained by multi-photon ionization, which scales with the square of wavelength, and is negligible even at these intensities in the X-ray regime.

Second, resonant photo-pumping of K-shell electrons to the L shell (rather than to the continuum) is energetically permitted for ions with both a single and a double K-shell hole in the final state. Radiative decay of these states produces the resonance emission highlighted in Fig. 1. Such emission appears prominently for states with two holes in the K-shell (marked as V–X for X-ray excitation in the range 1,600–1,680 eV), as well as from highly ionized states with a single K-shell hole (emission from peaks X and XI at excitation energies around 1,580 eV). In particular, we note that several peaks are observed on resonance rather than just one, indicating that the collisional rates are similar to, or larger than, Auger recombination rates.

To further interpret our results, we have performed time-dependent population kinetics calculations, using the SCFLY code¹⁸. These

simulations provide atomic level populations, CSDs, emission spectra, total absorbed energies and electron temperatures. The calculations are based on a rate-equation model that includes sequential single-photon absorption, spontaneous and stimulated emission, collisional excitation, ionization and their inverses, as well as the effects of opacity via an escape-factor formalism. We plot the calculated spectra for four X-ray excitation energies compared with our experimental measurements in Fig. 2. The interaction processes leading to the observed emission from a specific charge state (VIII) are shown alongside for the four X-ray photon energies, illustrating the different pathways resulting from a combination of direct K-shell photoionization, electron collisional ionization and resonant K–L transitions. We note that the emission intensity from the various charge states is not trivially related to the population of those charge states.

The simulated spectra successfully reproduce the experimental trends in a qualitative manner, however, quantitative differences can still be observed for several charge state emission intensities. This is in part due to uncertainties in the experimental intensity distribution on target, which is challenging to accurately account for (illustrated by the two simulation curves in Fig. 2, corresponding to different spatial profiles), in part to the simplifications made necessary for an efficient atomic-kinetics code, but mostly to uncertainties regarding fundamental physical parameters in warm and hot dense systems, such as the rates for inner-shell transitions, collisional ionization, Auger recombination in highly ionized hollow atoms, and the ionization potential depression. This last point regarding physical parameters is particularly acute in the case of emission from double-core-hole states, where the agreement between experiment and simulation is poorest. Nonetheless, given the qualitative agreement with the spectra and the straightforward energy absorption mechanism, the combined effect of these uncertainties on the basic thermodynamic quantities is not expected to be significant. The calculated electron temperature, free-electron density and CSD are shown in Fig. 3. Temperatures in excess of 100 eV are found, which do not depend strongly on the excitation wavelength. Further, higher X-ray photon energies invariably yield higher temperatures by the end of the pulse, despite having an initially lower absorption cross-section. This can be explained by thermal collisions governing the CSD: as the temperature rises, low charge states are depleted and higher-energy X-rays, which couple more efficiently to higher charge state transitions, deposit more energy in the system. To quantitatively evaluate this collisional effect, we illustrate in Fig. 4 the photoionization, Auger recombination and collisional ionization rates as a function of time for transitions populating and de-populating the single-core-hole charge state VII. We observe that by the peak of the pulse, at temperatures above 100 eV, electron–ion collisional

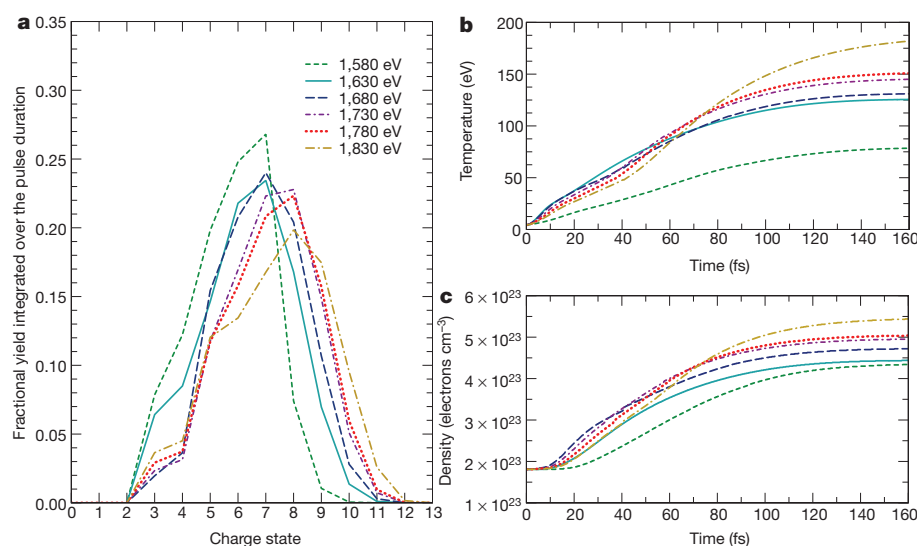


Figure 3 | Temperature, density and charge state distribution at peak intensity. **a**, Calculated charge state distribution, integrated over the duration of a temporally Gaussian pulse. The calculations correspond to the centre of the X-ray spot, at the highest spatial intensities. **b**, **c**, The temperature (**b**) and density (**c**) of the electronic system over a range of excitation energies. The peak of the X-ray pulse is centred at 80 fs, with a FWHM of 80 fs.

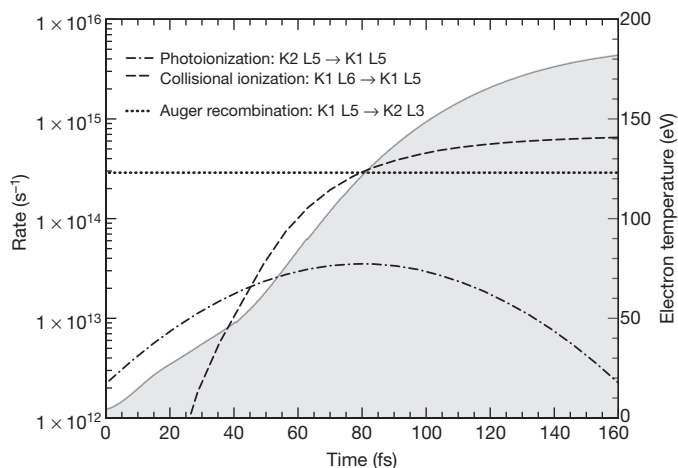


Figure 4 | Rates for atomic and collisional processes. Comparison between K-shell photoionization, collisional ionization and Auger recombination rates (broken curves, left-hand vertical axis) involved in populating and depopulating charge state VII at an X-ray photon energy of 1,830 eV. This state is one of the most populated for conditions leading to a peak temperature of ~ 100 eV. The calculation is conducted with a Gaussian beam (80 fs FWHM) centred at 80 fs. The electron temperature is given by the solid curve with grey shading under (right-hand vertical axis). By the peak of the pulse at 80 fs, the collisional ionization rate exceeds all others, dominating the population dynamics.

processes dominate the evolution of the CSD, and the dynamics of the system is determined by its temperature rather than by the intense X-ray excitation field. This result is fully consistent with our experimental results shown in Fig. 1.

Finally, in the context of creating well-defined states of matter in extreme conditions, we note that the duration of the pulse, heating of the electrons, photoionization and Auger decay are all rapid processes compared with atomic motion and hydrodynamic expansion of the target. For example, an aluminium ion at 150 eV travels only 5 nm in 100 fs, and thus a crude estimate of the hydrodynamic expansion time would be 20 ps for a 1 μm target. Given that electron-ion relaxation times are expected to be less than 10 ps (ref. 19), these results bode well for the creation of uniform-density hot and warm dense matter.

METHODS SUMMARY

A schematic illustration of the experimental set-up is given in Supplementary Fig. 1. The spectroscopy was conducted by means of a flat ammonium dihydrogen phosphate crystal (ADP) in the (101) orientation with a spectral resolution of 0.9–1.3 eV across the photon energy range of interest. All spectroscopic data were collected in single-shot acquisition mode, with a fresh region of the target exposed for every shot. Figure 1 was obtained by binning a total of around 550 single-shot spectra according to the measured X-ray photon energy in 5-eV bins.

Simulations of the experimental emission were conducted using an adapted version of the collisional-radiative code SCFLY¹⁸, which is based on the widely available FLYCHK simulation suite²⁰. SCFLY solves the rate equations for non-LTE (local thermal equilibrium) plasmas using a super-configuration description of the atomic structure of the system and provides a spectral module, which uses the computed level populations to calculate the X-ray emission spectra. Several important improvements have been included to make SCFLY applicable to X-ray FEL-driven systems: an increased number of super-configurations, the inclusion of hollow atoms and a self-consistent, absorption-driven temperature calculation. Each calculation provides an emission spectrum for a single X-ray intensity. To account for the experimental intensity distribution on target, 26 simulations covering the full range of probed intensities were computed for each X-ray excitation energy. The final spectra are obtained by averaging these over the three-dimensional interaction region, weighted according to the intensity distribution profile measured by the imprints technique in lead tungstate (PbWO₄). This intensity distribution, named the F-scan profile, which is obtained following the method described in ref. 9, is compared to the Gaussian intensity distribution consistent with the measured spot size (full-width at half-maximum, FWHM) in Fig. 2.

Full Methods and any associated references are available in the online version of the paper at www.nature.com/nature.

Received 27 August; accepted 29 November 2011.

Published online 25 January 2012.

1. Taylor, R. J. *The Stars: Their Structure and Evolution* 2nd edn (Cambridge Univ. Press, 1994).
2. Chabrier, G. Plasma physics and planetary astrophysics. *Plasma Phys. Contr. Fusion* **51**, 124014 (2009).
3. Helled, R., Anderson, J. D., Podolak, M. & Schubert, G. Interior models of Uranus and Neptune. *Astrophys. J.* **726**, 15 (2011).
4. Lindl, J. Development of the indirect-drive approach to inertial confinement fusion and the target physics basis for ignition and gain. *Phys. Plasmas* **2**, 3933–4024 (1995).
5. Remington, B. A., Drake, R. P. & Ryutov, D. D. Experimental astrophysics with high power lasers and Z pinches. *Rev. Mod. Phys.* **78**, 755–807 (2006).
6. Nagler, B. et al. Turning solid aluminium transparent by intense soft X-ray photoionization. *Nature Phys.* **5**, 693–696 (2009).
7. Linac Coherent Light Source. <https://lcls.slac.stanford.edu> (2011).
8. Young, L. et al. Femtosecond electronic response of atoms to ultra-intense X-rays. *Nature* **466**, 56–61 (2010).
9. Chalupský, J. et al. Spot size characterization of focused non-Gaussian X-ray laser beams. *Opt. Express* **18**, 27836–27845 (2010).
10. Bambynek, W. et al. X-Ray fluorescence yields, Auger, and Coster-Kronig transition probabilities. *Rev. Mod. Phys.* **44**, 716–813 (1972).
11. Saemann, A. et al. Isochoric heating of solid aluminum by ultrashort laser pulses focused on a tamped target. *Phys. Rev. Lett.* **82**, 4843–4846 (1999).
12. Rossall, A. K. et al. X-ray back-lighter characterization for iron opacity measurements using laser-produced aluminium K-alpha emission. *J. Phys. At. Mol. Opt. Phys.* **43**, 155403 (2010).
13. Bailey, J. et al. Observation of K α X-ray satellites from a target heated by an intense ion beam. *Laser Part. Beams* **8**, 555–562 (1990).
14. Burnett, N. H., Enright, G. D., Avery, A., Loen, A. & Kieffer, J. C. Time-resolved K α spectra in high-intensity laser-target interaction. *Phys. Rev. A* **29**, 2294–2297 (1984).
15. Back, C. A. et al. Study of K α absorption structures in a subcritical-density laser-produced plasma. *Phys. Rev. A* **46**, 3405–3412 (1992).
16. Rousse, A. et al. Efficient K α x-ray source from femtosecond laser-produced plasmas. *Phys. Rev. E* **50**, 2200–2207 (1994).
17. Gauthier, J.-C. et al. Theoretical and experimental studies of laser-produced plasmas driven by high-intensity femtosecond laser pulses. *Phys. Plasmas* **4**, 1811–1817 (1997).
18. Chung, H.-K., Chen, M. H. & Lee, R. W. Extension of atomic configuration sets of the non-LTE model in the application to the K α diagnostics of hot dense matter. *High Energy Density Phys.* **3**, 57–64 (2007).
19. Siwick, B. J., Dwyer, J. R., Jordan, R. E. & Miller, R. J. D. An atomic-level view of melting using femtosecond electron diffraction. *Science* **302**, 1382–1385 (2003).
20. Chung, H.-K., Chen, M. H., Morgan, W. L., Ralchenko, Y. & Lee, R. W. FLYCHK: Generalized population kinetics and spectral model for rapid spectroscopic analysis for all elements. *High Energy Density Phys.* **1**, 3–12 (2005).
21. Stewart, J. C. & Pyatt, K. D. Jr. Lowering of ionization potentials in plasmas. *Astrophys. J.* **144**, 1203–1211 (1966).
22. Chung, H.-K., Lee, R. W., Chen, M. H. & Ralchenko, Y. *The How To for FLYCHK* (NIST, 2008).

Supplementary Information is linked to the online version of the paper at www.nature.com/nature.

Acknowledgements Portions of this research were carried out on the SXR instrument at the LCLS, a division of SLAC National Accelerator Laboratory and an Office of Science user facility operated by Stanford University for the US Department of Energy. The SXR instrument and the Resonant Coherent Imaging (RCI) endstation are funded by a consortium whose membership includes the LCLS, Stanford University through the Stanford Institute for Materials Energy Sciences (SIMES), Lawrence Berkeley National Laboratory (LBNL), University of Hamburg through the BMBF priority programme FSP 301, and the Center for Free Electron Laser Science (CFEL). S.M.V., O.C. and J.S.W. thank the UK EPSRC for funding (EP/F020449/1 and EP/H035877/1). B.I.C., K.E., R.W.F. and P.A.H. acknowledge US DOE Basic Energy Science contract DE-AC03-76SF00098 and SSAA programme contract DE-FG52-06NA26212. T.B., J.C., L.J. and L.V. appreciate funding by grants LC510, LC528, LA08024, ME10046, P108/11/1312, P205/11/0571, IAX00100903 and KAN300100702. U.Z. thanks the German Ministry for Education and Research (BMBF) for funding under FSP 301. C.D.M. was supported by UK EPSRC (EP/G007187/1). We also thank G. Gregori (Oxford University) for discussions.

Author Contributions S.M.V., B.I.C., K.E., C.R.D.B., A.H., H.J.L., C.D.M., Y.P., S.T., U.Z., P.A.H., B.N. and J.S.W. performed the experiment and acquired the data. B.I.C., K.E., R.W.F. and P.A.H. analysed the data. S.M.V., O.C., H.-K.C., R.W.L. and J.S.W. performed the theoretical work. S.M.V., R.W.L. and J.S.W. wrote the paper. M.M., W.S. and J.J.T. operated the SXR beamline and the LCLS diagnostics. C.G., A.S., T.W., B.W. and D.Z. operated the RCI endstation. T.B., J.C., V.H., L.J., J.K. and L.V. performed the spot-size characterisation and analysis. All authors contributed to the work presented here and to the final paper.

Author Information Reprints and permissions information is available at www.nature.com/reprints. The authors declare no competing financial interests. Readers are welcome to comment on the online version of this article at www.nature.com/nature. Correspondence and requests for materials should be addressed to S.M.V. (sam.vinko@physics.ox.ac.uk).

METHODS

Experimental set-up. During the experiment, the total pulse energy was recorded on a shot-to-shot basis using a gas detector in the LCLS front-end enclosure. We measured an average pulse energy of 0.8–1.4 mJ, depending on the photon wavelength. Approximately 30–34% of this energy is delivered to the target owing to the transmission of the beamline optics between the gas detector and the Resonant Coherent Imaging (RCI) experimental chamber²³. During the course of the experiment, we scanned a photon energy range of 1,580–1,830 eV. The photon energy values are derived from the electron beam energies provided by the LCLS online diagnostics, the values of which were calibrated at the Al K edge both before and after the data acquisition. This method provides an accuracy of better than 5 eV in the absolute calibration, and is approximately constant over the entire range of energies investigated.

Data analysis. The noise filtering for the data analysis was conducted by analysing the number of counts per CCD (charge-coupled device) pixel: photons of 1,600 eV are seen to produce approximately 150 counts above the thermal noise level on the CCD detector, which is sufficient to isolate the signal and reduce the noise considerably. Any change in beam position on the sample will alter the crystal diffraction angle slightly, causing a shift in where wavelengths are mapped on to the detector. We have accounted for this positioning jitter effect by cross-correlating each single shot with the average spectrum and adjusting the positions of the K α satellite peaks accordingly to overlap. The wavelength axis of the final spectrum is then calibrated by fitting the positions of the main K α peak and its satellites to previously published values¹³. This eliminates the need to use geometric considerations to map the detector pixels to wavelength and is considerably more accurate. We did not measure the temporal profile of the LCLS beam or the pulse length. Instead, the LCLS electron bunch length was measured (80 fs FWHM) and assumed to be a good indication of the X-ray pulse duration. However, this value should only be considered as an upper bound on the pulse duration, with recent experiments reporting results consistent with 2–3 times shorter pulses^{8,24}.

Modelling. Simulations of the experimental emission were conducted using the SCFLY code^{18,20} adapted to simulate FEL-driven systems. It has recently been reported that these modifications enable SCFLY to successfully simulate X-ray–matter interactions in the non-collisional regime limit²⁵. For the work presented here, which extends this study to the highly collisional regime, a complete set of super-configurations for all ionic species of aluminium up to the $n = 3$ shell are considered in the code. We have further verified that the spectrum exhibits a negligible dependence on the temporal structure of the X-ray pulse, provided the total fluence is constant, by comparing calculated spectra obtained by using a Gaussian temporal profile with a simulated self-amplified spontaneous emission FEL pulse of equal duration and fluence, following ref. 26.

The energies used in the simulations are calculated according to the relativistic configuration average model following a Dirac–Hartree–Slater method²⁷. The agreement in peak position that can be observed between simulation and experiment, within ~ 3 eV (0.2%) for the highest charge states, was deemed sufficient within the context of our investigation. It can however be improved on by using a fine structure model for the energy levels, albeit at a significant additional computational cost.

23. Sorokin, A. A., Jastrow, U., Juranić, P., Kapitzki, S. & Tiedtke, K. *Report on Pulse Energy Monitoring at the SXR Beamline Using Gas-Monitor Detectors* (Technical report, SLAC, 2010).
24. Düsterer, S. *et al.* Femtosecond x-ray pulse length characterization at the Linac Coherent Light Source free-electron laser. *New J. Phys.* **13**, 093024 (2011).
25. Ciricosta, O., Chung, H.-K., Lee, R. W. & Wark, J. S. Simulations of neon irradiated by intense X-ray laser radiation. *High Energy Density Phys.* **7**, 111–116 (2011).
26. Bonifacio, R., De Salvo, L., Pierini, P., Piovella, N. & Pellegrini, C. Spectrum, temporal structure, and fluctuations in a high-gain free-electron laser starting from noise. *Phys. Rev. Lett.* **73**, 70–73 (1994).
27. Chen, M. H., Crasemann, B. & Mark, H. Relativistic K-shell Auger rates, level widths, and fluorescence yields. *Phys. Rev. A* **21**, 436–441 (1980).